AIAA JOURNAL
Vol. 30, No. 4, April 1992

Flow Past a Wing-Body Junction—Experimental Evaluation of Turbulence Models

William J. Devenport* and Roger L. Simpson†
Virginia Polytechnic Institute and State University, Blacksburg, Virginia 24061

Detailed three-component laser Doppler velocimeter measurements have been made in the flow of a turbulent boundary layer past an idealized wing-body junction. These measurements, which show great variety and three dimensionality in the vortex-dominated turbulence structure of this flow, are here used to evaluate the closure assumptions of a number of turbulence models. Many of these models require or imply a relationship between the angles of the turbulence shear-stress and mean-velocity vectors. In the present flow, these angles are not only different but do not follow any simple relationship. To predict the shear-stress angle, accurate modeling of the full shear-stress transport equations is clearly needed. In particular, new models based on measurements are needed for the pressure-strain term. The closure assumptions of six turbulence models are tested by using them to predict the magnitude of the shear-stress vector from the mean-velocity and/or turbulence kinetic energy. Among the best are those of the Cebeci-Smith and algebraic-stress models. The k-ε model does not appear suited to this vortical flow.

Introduction

THIS paper follows several papers[1-6] in which we have presented detailed velocity measurements made in the flow of a turbulent boundary layer around the nose of a wing-body junction. The purposes of this paper are 1) to briefly review these measurements, 2) to present new measurements made around the rest of the junction, and 3) to use the whole data set to evaluate the usefulness and generality of a variety of turbulence models and modeling parameters.

For a review of other experimental work on wing-body junction flows see Devenport and Simpson.[6]

Equipment

Only abbreviated descriptions are given here; for complete details see Devenport and Simpson.[7]

Wing and Wind Tunnel

The wing (Fig. 1) is cylindrical, has a maximum thickness T of 71.7 mm, a chord of 305 mm, and a span of 229 mm. In cross section, its shape (Fig. 2) consists of a 3:2 elliptical nose (major axis aligned with the chord) and a NACA 0020 tail joined at the maximum thickness. Trips are attached to both sides of the wing to ensure steady and fixed transition.

The wing is mounted at zero sweep and incidence at the center of the flat 0.91-m-wide test wall of the Virginia Tech Boundary Layer Tunnel, forming the junction. In the absence of the wing, this tunnel produces a flow of zero streamwise pressure gradient, consisting of a closely uniform (to within 1%) low-turbulence (0.2%) freestream and an equilibrium two-dimensional turbulent boundary layer[8] on the test wall. With the wing in place, inserts attached to the wind-tunnel side walls are used to minimize blockage-induced pressure gradients.

Laser Doppler Velocimeter

A three-component laser Doppler velocimeter (LDV) was used to measure detailed profiles of mean-velocity and turbulence quantities in six planes surrounding the wing. These planes (numbered 1, 3, 4, 5, 8, and 10 for organizational reasons) are illustrated in Fig. 2.

The LDV has three sets of sending optics, two of which are shown schematically in Fig. 1. Each set produces an arrangement of beams sensitive to a different pair of velocity components and their associated Reynolds shear stress. Only one set is used at a time. The flow is seeded using dioctal phthalate smoke (typical particle diameter 1 μ). Light scattered from the measurement volume is focused onto the pinhole of a single photomultiplier tube. Data are obtained from the photomultiplier signal using either fast sweep rate sampling spectrum analysis[9] or a DANTEC 55N10 Burst Spectrum Analyzer. Velocity statistics are obtained by time (not particle) averaging and, thus, should be free of bias.

Measurements presented here have been corrected, where necessary, for velocity gradient broadening and finite transit time broadening using the techniques described by Durst et al.[10] Uncertainty estimates for 95% confidence limits are listed in Table 1.

Coordinate Systems, Test Conditions

Most results and discussion will use the lab fixed coordinate system X, Y, Z and U, V, W centered at the intersection of the wing leading edge and wall (Fig. 1). X is measured downstream from the leading edge, Y normal to the wall, and Z completes a right-handed system. In presenting LDV measurements, the additional coordinate S will be used. S is measured along any of the LDV measurement planes from the wing surface or flow centerline, as shown in Fig. 2. In discussing turbulence models and parameters, other coordinate systems will be used, distinguished by subscripts. Subscripts f, s, and g refer coordinates fixed in the local freestream direction, the local mean-flow direction, and the local direction of the mean-velocity gradient vector, respectively. In calculating these directions, V component velocities will be ignored. In all coordinate systems, upper- and lower-case symbols will be used to denote the mean and fluctuating components of velocity, respectively.

Distances will in general be nondimensionalized on the maximum thickness of the wing T and velocities on the undisturbed approach freestream velocity U_{ref}. Under nominal test conditions, the momentum thickness Reynolds number of the approach boundary layer, measured in the plane of symmetry $2.15T$ upstream of the wing leading edge, was

Received Sept. 4, 1990; revision received April 26, 1991; accepted for publication April 27, 1991.

*Assistant Professor, Department of Aerospace and Ocean Engineering. Senior Member AIAA.
†Jack E. Cowling Professor, Department of Aerospace and Ocean Engineering. Fellow AIAA.

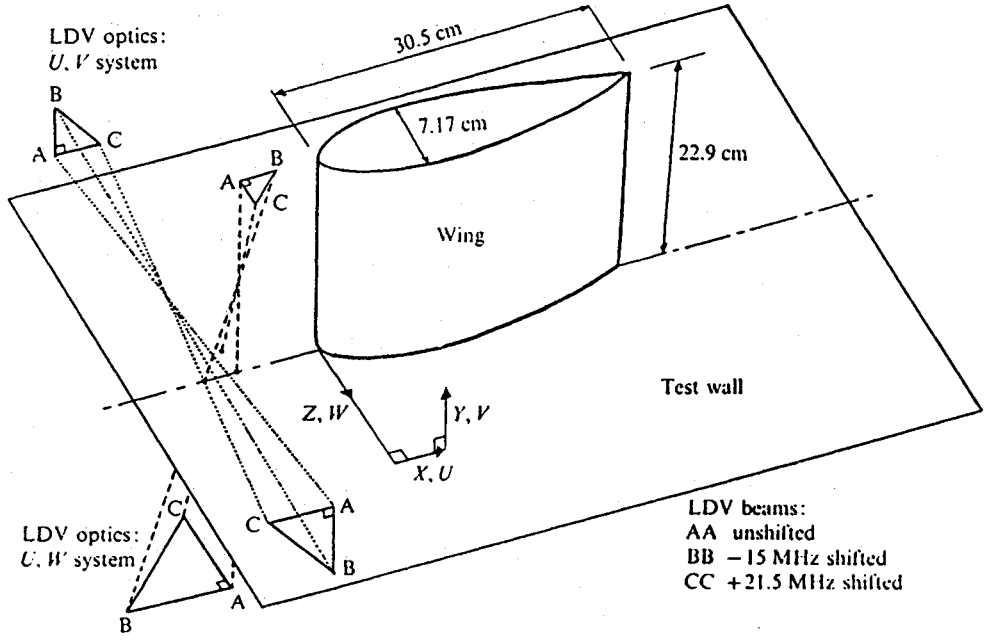

Fig. 1 Perspective view of the wing-body junction.

6.7×10^3, corresponding to a total boundary-layer thickness δ of 36 mm ($0.50T$) and U_{ref} of 27 m/s.

Experimental Results

Figure 2 shows contours of mean surface pressure coefficient C_p (based on undisturbed freestream conditions) and principle features of an oil-flow visualization performed on the wall surrounding the wing. Figures 3 and 4 show mean-velocity vectors and contours of turbulence kinetic energy k/U_{ref}^2 measured in planes 1–10. The mean-velocity vectors represent components normal to the centerline of the horseshoe vortex defined as the locus of peak turbulence kinetic energy (see Fig. 2). Other projections of the mean-velocity field (e.g., normal to the wing, parallel to the measurement planes) do not clearly show the secondary-flow velocities associated with the vortex. Note that the measurements presented here in planes 1, 3, and 4 have previously been published by Devenport and Simpson.[2–4,6]

This flow is dominated by the pressure field produced by the wing and the velocity field generated by the horseshoe vortex that is wrapped around the junction between the wing and wall. In the plane of symmetry upstream of the wing (plane 1), the oncoming boundary layer experiences an adverse pressure gradient that causes it to separate $0.47T$ upstream of the leading edge (Fig. 2). The separation region formed (Fig. 3a) is dominated by the recirculation associated with the horseshoe vortex. This roughly elliptical structure, centered at $X/T = -0.2$, $Y/T = 0.05$, generates an intense backflow by reversing fluid impinging on the leading edge of the wing. The backflow reaches a maximum mean velocity of $-0.48U_{ref}$ and then decelerates, giving the appearance of reseparation between $X/T = -0.25$ and -0.3. Reseparation, however, does not occur as a thin region of weak reversed flow is sustained adjacent to the wall. This region is then all that remains of the backflow upstream to the separation point. The near reseparation of the backflow produces a distinct line in the surface oil-flow visualization known as the line of low shear (Fig. 2).

In the vicinity of the horseshoe vortex, the turbulence stresses (and, thus, the turbulence kinetic energy) become very large reaching values an order of magnitude greater than in the approach boundary layer (Fig. 4a). These large stresses are

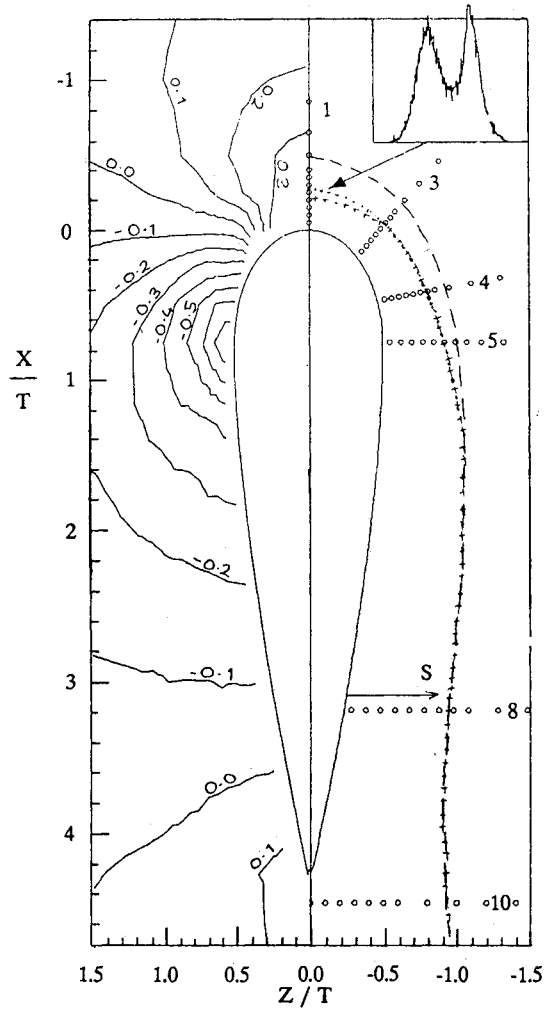

Fig. 2 Contours of mean surface pressure coefficient C_p on the wall surrounding the wing: ○ locations of LDV profiles; —— line of separation; ···· line of low shear; + + + + locus of peak turbulence kinetic energy in the vortex (inset: histogram of U component velocity fluctuations measured at $X/T = -0.2$, $Y/T = 0.005$, $Z/T = 0.0$).

associated with bimodal (double-peaked) histograms of velocity fluctuations, like the inset in Fig. 2, and are produced by intense low-frequency bistable unsteadiness in the structure of the vortex. This unsteadiness is a result of the turbulent/nonturbulent intermittency of fluid entrained into the corner between the wing and wall.[6]

Moving out of the plane of symmetry, fluid experiences a strong favorable pressure gradient (Fig. 2) that accelerates as it moves around the nose. Close to the wing in planes 3, 4, and 5 this acceleration, acting in concert with the rotational motion of the vortex (which here is bringing low-turbulence high-momentum fluid from the freestream down close to the wall), locally relaminarizes the boundary layer.[4,5] Turbulence shear stresses in this region are, therefore, much smaller than elsewhere. Turbulence kinetic energy (Figs. 4b–4d) is also reduced. Although the intensity of turbulent fluctuations in the vicinity of the vortex falls in the favorable pressure gradient, the peak values of turbulence kinetic energy remain many times those in the surrounding boundary layer because of the bimodal unsteadiness. Bimodal histograms are seen in the vicinity of the vortex in planes 3, 4, and 5 (Figs. 4b–4d). Despite the favorable pressure gradient, the vortex clearly grows in this region moving away from the wall and the wing (Figs. 3 and 4). (Projected onto the wall, the centerline of the vortex fairly closely follows the line of low shear, see Fig. 2.) In addition, mean secondary flow velocities fall by a factor of about 2 between planes 1 and 5 (Fig. 3).

Downstream of the maximum thickness, this flow is subjected to an adverse pressure gradient (Fig. 2) that appears to cause rapid growth in the vortex and a dissipation of the bimodal unsteadiness. (Note the change in scales between different parts of Figs. 3 and 4.) Bimodal histograms were not observed in planes 8 and 10, and peak turbulence kinetic energies are much lower here than upstream. Secondary-flow velocities, which are also reduced in the adverse pressure gradient, become much more difficult to distinguish from the rest of the mean-velocity field (Figs. 3e and 3f). Despite these changes, the region between the vortex and the wing remains one of low-turbulence shear stresses because of the freestream fluid entrained here by the vortex.

Table 1 Typical uncertainties in LDV measurements (95% confidence limits)

Quantity	Uncertainty
Mean velocity	$\pm 0.03\ U_{ref}$
Turbulence kinetic energy k	$\pm 0.00026\ U_{ref}^2$
Turbulence shear stress $-\overline{uv}$	$\pm 0.00033\ U_{ref}^2$
Turbulence shear stress $-\overline{vw}$	$\pm 0.00027\ U_{ref}^2$
Turbulence shear-stress magnitude	$\pm 0.00033\ U_{ref}^2$

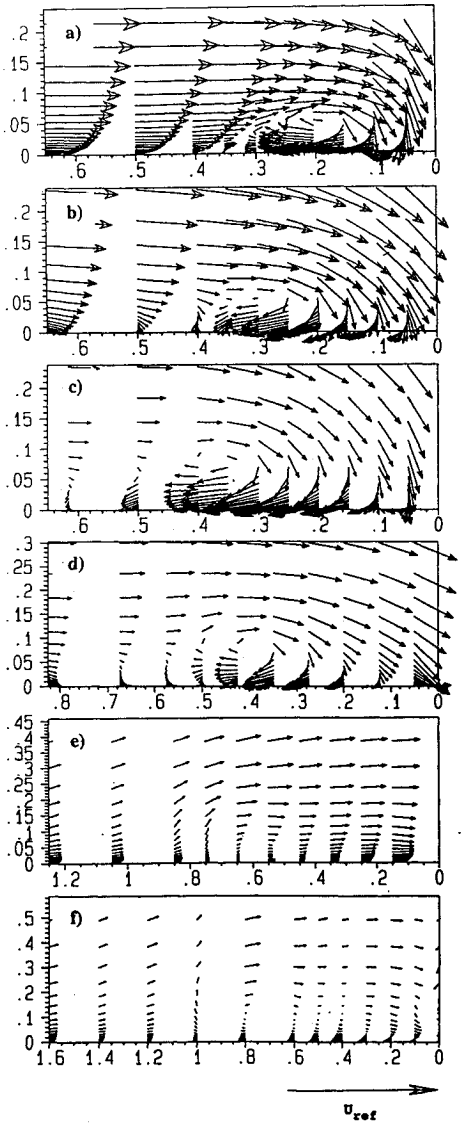

Fig. 3 Mean secondary flowfield generated by the vortex: a) plane 1; b) plane 3; c) plane 4; d) plane 5; e) plane 8; f) plane 10.

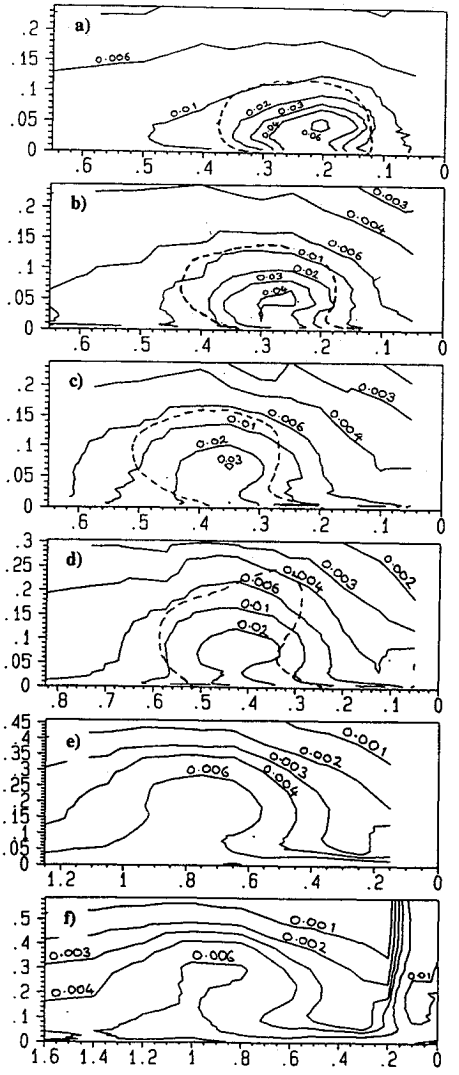

Fig. 4 Contours of turbulence kinetic energy k/U_{ref}^2 in the vicinity of the vortex; dotted lines enclose the regions in which bimodal histograms are observed: a) plane 1; b) plane 3; c) plane 4; d) plane 5; e) plane 8; f) plane 10.

Figures 3 and 4 represent only a fraction of the mean-velocity and turbulence information we have collected. All mean-velocity and Reynolds stress components, some triple products, and histograms of fluctuations in all three components have been measured at over 1400 points in this flow. The quantity of experimental data and the variety of turbulence structure in this flow make it, in our opinion, ideal for testing the generality and, therefore, usefulness of turbulence models.

Evaluation of Turbulence Models

General Remarks

Before addressing specific turbulence models, it is appropriate to discuss the relationship between the turbulent shear stress and velocity gradient directions since many models use or imply such a relationship. The shear-stress and velocity-gradient vectors are defined as having components $-\overline{uv}$, $-\overline{vw}$ and $\partial U/\partial Y$, $\partial W/\partial Y$ in the X and Z directions, respectively. Their directions are given by the angles,

$$\alpha_t = \tan^{-1}\left(\frac{-\overline{vw}}{-\overline{uv}}\right), \qquad \alpha_g = \tan^{-1}\left(\frac{\partial W/\partial y}{\partial U/\partial y}\right) \tag{1}$$

Most often the shear-stress and velocity gradient angles are assumed to be the same, i.e.,

$$\frac{-\overline{vw}}{-\overline{uv}} = \frac{\partial W/\partial Y}{\partial U/\partial Y} \quad \text{or} \quad \frac{-\overline{uv}}{\partial U/\partial Y} = \frac{-\overline{vw}}{\partial W/\partial Y} \tag{2}$$

As shown, this implies that the streamwise and crossflow eddy viscosities are the same. Although this is ideal for converting turbulence models designed for two-dimensional flows to three dimensions, it is not supported by the present or past[11-13] experiments. Figure 5 shows a plot of spanwise vs streamwise eddy viscosity for all points inside the boundary layer in planes 3–10. Points outside the line of separation, where the direct effects of the horseshoe vortex and its bimodal unsteadiness are much smaller, are plotted with different symbols to those inside. There does not appear to be any significant correlation between these two parameters in either region.

A possible improvement has been suggested by Rotta,[14] who derives an alternative relationship between the eddy viscosities using the transport equations for the shear stresses approximated for thin shear layers,

$$\frac{\mathrm{D}(-\overline{uv})}{\mathrm{D}t} = \overline{v^2}\frac{\partial U}{\partial Y} - \overline{\frac{p'}{\rho}\left(\frac{\partial u}{\partial Y} + \frac{\partial v}{\partial X}\right)} + \frac{\partial}{\partial y}\left(\overline{\frac{p'u}{\rho}} + \overline{uv^2}\right) \tag{3}$$

$$\frac{\mathrm{D}(-\overline{vw})}{\mathrm{D}t} = \overline{v^2}\frac{\partial W}{\partial Y} - \overline{\frac{p'}{\rho}\left(\frac{\partial w}{\partial Y} + \frac{\partial v}{\partial Z}\right)} + \frac{\partial}{\partial y}\left(\overline{\frac{p'w}{\rho}} + \overline{wv^2}\right) \tag{4}$$

The terms from left to right represent convection, production, pressure strain, and diffusion. By substituting the Poisson equation for the fluctuating pressure p', it can be shown that the pressure strain is composed of two terms: the first Φ_1 is associated with the interaction of the mean strain and fluctuating velocities, and the second Φ_2 with the interaction of the fluctuating velocities alone. Φ_2 is usually approximated by the shear stress itself multiplied by a factor related to the turbulence kinetic energy,[15] which is the same in both equations. Rotta approximated Φ_1 using the Poisson equation for the pressure fluctuation and by assuming local symmetry in the turbulence structure. Neglecting convection and diffusion, which can be shown to be higher order terms for thin shear layers, and dividing Eqs. (2) by Eqs. (1) he then obtained the expression,

$$\tan(\alpha_t - \alpha) = T.\tan(\alpha_g - \alpha) \quad \text{or}$$

$$\frac{-\overline{v_s w_s}}{\partial W_s/\partial Y} = T.\frac{-\overline{u_s v_s}}{\partial U_s/\partial Y} \tag{5}$$

i.e., the spanwise eddy viscosity is an empirical constant T times the spanwise eddy viscosity, in local mean-flow coordinates. Unfortunately, as can be seen from Fig. 5 these equations are no more valid than Eqs. (2) in the present flow.

We have tested a number of other hypothetical relationships between the shear-stress and velocity gradient angles also without success. These have included a relationship between $\alpha_t - \alpha_g$ and the local crossflow velocity W_f/U_e, one between the spanwise and streamwise eddy viscosities, and one between α_t and α_g based on van den Berg's[16] hypothesis.

There are two principle reasons for the failure of these concepts. The first becomes apparent if we transform the problem to coordinates based on the direction of the local mean velocity gradient vector (subscript g). In this system, the crossflow shear stress exactly represents the lag or lead of the angle of the shear-stress vector over that of the velocity gradient vector, i.e.,

$$\frac{-\overline{vw_g}}{-\overline{u_g v}} = \tan(\alpha_t - \alpha_g) \tag{6}$$

Also in this system, however, the transport equations for the crossflow stress [Eq. (4)] loses the term $\overline{v^2}\,\partial W/\partial Y$ since by definition $\partial W/\partial Y$ is zero. The crossflow stress and the lag of the shear-stress vector are therefore determined entirely by the unknown pressure strain and the neglected convection and diffusion terms, which in the absence of $\overline{v^2}\,\partial W/\partial Y$ are likely to be important. The second reason for the failure is the way in which the pressure strain terms are usually mod-

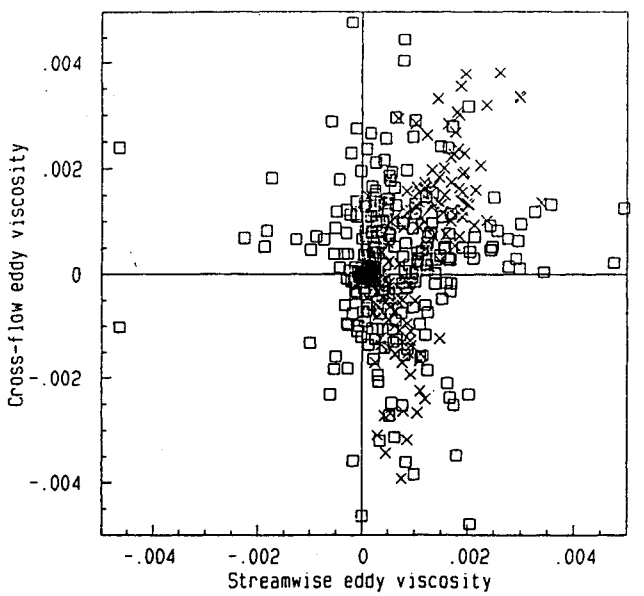

Fig. 5 Spanwise vs streamwise eddy viscosity in local mean flow coordinates for all measurement points inside the boundary layer ($\sqrt{u^2}/U > 5\%$): squares represent points outside the line of separation.

eled. It is simple to show that (without the boundary-layer approximation) the pressure strain and pressure diffusion can be combined into a single term with the form,

$$-\overline{v\frac{\partial p'}{\partial X} + u\frac{\partial p'}{\partial Y}} \tag{7}$$

in the $\overline{uv}$ transport equation, and

$$-\overline{v\frac{\partial p'}{\partial Z} + w\frac{\partial p'}{\partial Y}} \tag{8}$$

in the $\overline{vw}$ transport equation. These terms obviously cannot be modeled by substituting for $\partial p'/\partial X$, $\partial p'/\partial Y$, and $\partial p'/\partial Z$ from the Navier-Stokes equations or an approximation to them (as done by van den Berg[16]) since this will lead to an identity or an expression of the error in the approximation. By the same argument, substituting for p' using the Poisson equation (which is just the Navier-Stokes rearranged) or an approximation (as is done in effect by Rotta[14]) must similarly lead to an invalid result.

The pressure strain terms can in general only be modeled by substituting different moments of Navier-Stokes equations and/or by using information derived from experiments. In our opinion, only the latter approach is likely to prove successful since higher moments of the Navier-Stokes will only introduce more unknowns. Careful experiments in which the pressure strain terms are (presumably) measured by difference are, therefore, needed.

Turbulence Models

In this section, the assumptions of several prescribed eddy viscosity models, the k-ε model, an algebraic-stress model, and Bradshaw's[17] model are tested. For each model, predictions of the magnitude of the shear-stress vector from the measured mean-velocity or turbulence kinetic energy distributions are compared with measurements. For models that use the eddy viscosity ν_t, the shear-stress magnitude is assumed to be given by

$$(\overline{uv}^2 + \overline{vw}^2)^{1/2} = \nu_t\left[\left(\frac{\partial U}{\partial Y}\right)^2 + \left(\frac{\partial W}{\partial Y}\right)^2\right]^{1/2} \tag{9}$$

i.e., the crossflow and streamwise eddy viscosities are assumed equal. Although the results of the preceding section show that this is not the case, there appears to be no better alternative. Since skin-friction data are not yet available for the present flow, the wall treatments employed by most of the models are not tested and are ignored in the following discussion. Comparisons with experimental data do not include points in the near-wall region $Y/T < 0.02$ ($y^+ < \sim 120$).

The authors concede that several of the models examined here were never intended for use in flows as complex as this one. However, they, or models like them, are often used in complex flows. It is, therefore, important that their limitations be known.

In the first and simplest turbulence model considered here, the eddy viscosity is prescribed as a function of Y entirely in terms of mixing length l,

$$l = \kappa Y \qquad Y/\delta < \lambda/\kappa \tag{10a}$$

$$l = \lambda\delta \qquad Y/\delta \geq \lambda/\kappa \tag{10b}$$

where the eddy viscosity is given by

$$\nu_t = l^2\left[\left(\frac{\partial U}{\partial Y}\right)^2 + \left(\frac{\partial W}{\partial Y}\right)^2\right]^{1/2} \tag{11}$$

where λ and κ are empirical constants, given their normal values of 0.09 and 0.4, and δ is the boundary-layer thickness.

The Cebeci-Smith and Johnston-King turbulence models, described for three-dimensional flows by Abid,[18] are variations on this basic form. The Cebeci-Smith model is given by the relations

$$\nu_t = \nu_{t_o}\left[1 - \exp(-\nu_{t_i}/\nu_{t_o})\right] \tag{12}$$

where

$$\nu_{t_i} = l^2\left[\left(\frac{\partial U}{\partial Y}\right)^2 + \left(\frac{\partial W}{\partial Y}\right)^2\right]^{1/2} \qquad l = \kappa Y, \quad \kappa = 0.4 \tag{13}$$

and

$$\nu_{t_o} = 0.0168\gamma_\kappa\left|\int_0^\delta (Q_e - Q)\,dy\right| \tag{14}$$

$$\gamma_\kappa = \left[1 + 5.5\left(\frac{Y}{\delta}\right)^6\right]^{-1} \tag{15}$$

$$Q = \sqrt{U^2 + W^2}: \qquad Q_e = Q|_{Y=\delta} \tag{16}$$

the principal difference with the basic model being the explicit prescription of the eddy viscosity in the outer region in terms of the Klebanoff intermittency function γ_k and the use of a smoothing function between the inner and outer regions. The Johnson-King model uses the same smoothing function but defines

$$\nu_{t_i} = l\sqrt{\tau_m} \qquad l = \kappa Y, \quad \kappa = 0.4 \tag{17}$$

and

$$\nu_{t_o} = 0.0168\sigma\gamma_\kappa\left|\int_0^\delta (Q_e - Q)\,dy\right| \tag{18}$$

where

$$\tau_m = (\overline{uv}^2 + \overline{vw}^2)^{1/2}|_m \tag{19}$$

the maximum turbulence shear stress in the profile. Note that, given the mean-velocity gradients, Eqs. (9), (12), and (17–19) constitute a relationship between τ_m and the nonequilibrium parameter σ since τ_m is a function of the eddy-viscosity distribution as well as one of its inputs. To determine τ_m and σ, a second relationship is needed. This comes in the form of an approximate differential transport equation for τ_m,

$$U_m\frac{\partial \tau_m}{\partial X} + W_m\frac{\partial \tau_m}{\partial Z} = \frac{a_1}{L_m}\tau_m(\sqrt{\tau_{m,\mathrm{eq}}} - \sqrt{\tau_m}) - \frac{C_D\tau_m^{3/2}|1-\sigma|}{0.7\delta - Y_m} \tag{20}$$

where a_1 and C_D are empirical constants given values of 0.25 and 0.5, respectively, subscript m denotes a value at the Y location of the maximum shear stress, and $\tau_{m,\mathrm{eq}}$ is the value of τ_m determined from Eqs. (9), (12), and (17–19) taking σ as 1.0. The Johnson-King model was originally designed for two-dimensional adverse pressure gradient and separated boundary layers in which the maximum shear stress appears to be an appropriate scaling parameter.

These three models were used to calculate the turbulence shear-stress magnitude from the measured mean-velocity field. In the case of the Johnson-King model, an iterative procedure was required to solve the eddy-viscosity and differential transport equations simultaneously. Note that convection of τ_m normal to the LDV measurement planes was ignored in these calculations.

The k-ε model is one of the most widely used in calculating two- and three-dimensional turbulent flows. Coupled with the wall treatment of Chen and Patel,[19] it has been used by Deng[20] to calculate the flow past a wing-body junction very similar to that studied in the present experiments. The k-ε model defines the eddy viscosity in terms of the turbulence kinetic energy k and the dissipation ε,

$$\nu_t = C_\mu \frac{k^2}{\varepsilon} \tag{21}$$

where k and ε are determined from approximate transport equations,[15,21]

$$\frac{Dk}{Dt} = -\overline{uv}\frac{\partial U}{\partial Y} - \overline{vw}\frac{\partial W}{\partial Y} - \varepsilon + \frac{\partial}{\partial Y}\left[\left(\nu + \frac{\nu_t}{\sigma_k}\right)\frac{\partial k}{\partial Y}\right] \tag{22}$$

$$\frac{D\varepsilon}{Dt} = -C_{\varepsilon 1}\frac{\varepsilon}{k}\left(\overline{uv}\frac{\partial U}{\partial Y} + \overline{vw}\frac{\partial W}{\partial Y}\right) - C_{\varepsilon 2}\frac{\varepsilon^2}{k} + \frac{\partial}{\partial Y}\left[\left(\nu + \frac{\nu_t}{\sigma_\varepsilon}\right)\frac{\partial \varepsilon}{\partial Y}\right] \tag{23}$$

The empirical constants are usually given the values,

$$C_\mu = 0.09, \quad \sigma_k = 1, \quad C_{\varepsilon 1} = 1.57$$

$$C_{\varepsilon 2} = 2.0, \quad \sigma_\varepsilon = 1.3 \tag{24}$$

The ε equation could not be tested using the present measurements. The k equation was tested by substituting the eddy-viscosity and the velocity gradients for the Reynolds stresses and substituting Eq. (21) for the dissipation. This gives

$$\frac{Dk}{Dt} = \nu_t\left[\left(\frac{\partial U}{\partial Y}\right)^2 + \left(\frac{\partial W}{\partial Y}\right)^2\right] - \frac{C_\mu k^2}{\nu_t} + \frac{\partial}{\partial Y}\left[\left(\nu + \frac{\nu_t}{\sigma_k}\right)\frac{\partial k}{\partial Y}\right] \tag{25}$$

Using the measured distributions of k and the mean-velocity gradients, this equation was solved iteratively for ν_t. Initial and boundary values for ν_t required for this calculation were determined from the measurements. Convection of k normal to the LDV measurement planes was ignored in this calculation since it could not be deduced from the measurements. This term was almost certainly negligible at most points.

The algebraic stress model uses transport equations for k and ε similar to those in Eqs. (22) and (23). However, instead of relating the turbulent stresses to k and ε through an eddy viscosity, algebraic equations for the individual stresses are used. These are derived from the full (differential) stress transport equations by assuming, among other things, that the convection and diffusion of the individual stresses is proportional to that of k. The algebraic stress equations, written in standard tensor notation in their full form,[15,21] are

$$\overline{u_i u_j} = (2/3)\delta_{ij}k + \frac{(1-\gamma)[(P_{ij}/\varepsilon) - (2/3)\delta_{ij}(P/\varepsilon)] + \Phi_{ijw}/\varepsilon}{C_1 + P/\varepsilon - 1}k \tag{26}$$

where P_{ij} is the production of $\overline{u_i u_j}$, P is the production of k, δ_{ij} is 1 of $i = j$ and zero otherwise, and Φ_{iiw} is a component of the pressure-strain correlation that accounts for wall proximity effects. Φ_{ijw} is an algebraic function of only k, ε, Y, and the stresses themselves.[21] The following values for the empirical constants, suggested by Abid and Schmitt[21] and Launder,[22] were used:

$$\gamma = 0.55, \quad C_1 = 2.2, \quad C_1' = 0.5, \quad C_2' = 0.3 \tag{27}$$

where C_1' and C_2' appear in the equations for Φ_{ijw}. Equation (26), together with the definition of k, give seven algebraic equations for the six Reynolds stresses and ε in terms of k and the mean-velocity field. If the latter are provided from experimental data, then the stresses and ε can be deduced. This requires an iterative Newton-Raphson procedure since the equations are nonlinear. Combining $\overline{uv}$ and $\overline{vw}$ then gives the magnitude of the shear stress. In performing this calculation, production terms associated with gradients of V and W normal to the measurement planes were ignored since they could not be obtained from the measurements. These terms were almost certainly negligible at most points. Note that Eq. (26) does not involve boundary-layer approximations. Without these, the algebraic stress model can, at least in theory, predict a lag or lead in the angle of the turbulence shear-stress vector.

Bradshaw's[17] turbulence model for three-dimensional boundary layers uses approximate differential transport equations for $\overline{uv}$ and $\overline{vw}$. These are derived by analogy with the transport equation for k assuming a simple constant of proportionality between k and the shear-stress magnitude,

$$a_1 = \frac{(\overline{uv}^2 + \overline{vw}^2)^{1/2}}{2k} \tag{28}$$

By analogy with two-dimensional flows, Bradshaw suggests a value of 0.15 for a_1. This relationship was tested by multiplying measured values of k by 0.15 to obtain estimates of the shear-stress magnitude.

Results

Results for the turbulence model calculations are presented in Figs. 6 and 7. Figures 6a–6h show measured and computed contours of shear-stress magnitude in plane 8 located toward the trailing edge of the wing (Fig. 2). Because of space limitations, detailed comparisons in other planes are not presented. However, Figs. 7b–7h show, for each turbulence model, histograms of the difference between computed and measured shear-stress magnitudes compiled from data in all planes. The filled portion of these histograms was compiled from positions outside the line of separation where the direct effects of horseshoe vortex and its bimodal unsteadiness are much smaller. The means and standard deviations of these histograms are listed in Table 2. Note that this representation of the error is effectively weighted toward those regions where the shear-stress magnitude is greatest and, therefore, its prediction is most important. For reference, Fig. 7a shows a histogram representing probable errors in the experimental data deduced from uncertainty estimates. Note that Figs. 7a–7g do not contain data from close to the wall ($Y/T < 0.02$) or from in the freestream ($\sqrt{u^2}/U < 5\%$).

Of the prescribed eddy-viscosity models (Figs. 6 and 7b–7d), the Cebeci-Smith appears to be the best in plane 8. Although there are some obvious qualitative differences in the shapes of the measured and computed shear-stress contours (compare Figs. 6a–6c), these do not represent large quantitative differences at most points. In other planes, there are some large differences, however, as indicated by the histograms in Fig. 7c. Although these histograms do not indicate much mean error (Table 2), the rms errors are large, being about 0.001 overall and 0.00077 outside the line of separation (2 and 1.5 contour levels in Fig. 6c, respectively).

In plane 8, the Johnson-King model (Fig. 6d) does not perform well, significantly underpredicting the shear-stress magnitude at most positions. The corresponding histograms (Fig. 7d) show, however, that this is not a problem in other planes because there is little overall mean error in the predictions of this model. The rms errors (Table 2) are slightly larger than those of the Cebeci-Smith model. It appears, therefore, that the Johnson-King gains little from its differential transport equation for the maximum shear stress and the use of the maximum shear stress in determining the eddy viscosity. This may simply be an indication that the location and magnitude of the maximum shear stress do not have as much physical significance in this flow as they do in separating two-dimensional boundary layers.

Although the shear-stress magnitude distributions produced by the basic mixing length model of Eqs. (10) and (11) appear qualitatively realistic (Fig. 6b), the histograms in this case (Fig. 7b) show large quantitative discrepancies (overall mean and rms errors +0.00064 and 0.0012, respectively). A detailed comparison with the measurements shows that most of the larger discrepancies occur in the near-wall region where the mixing length is prescribed as a linear function of Y [Eqs. (10)]. The only difference between this and the Cebeci-Smith model in this region [Eq. (13)] is the use of the smoothing function [Eq. (12)]. It therefore appears that this function is an important part of the Cebeci-Smith model.

Unlike the preceding models, the k-ε, algebraic-stress, and Bradshaw's[17] models were given the measured distribution of turbulence kinetic energy from which to calculate the shear-stress magnitude. It is surprising then that these models appear to perform little better (see Figs. 6 and 7e–7h).

The k-ε model does not accurately reproduce the features of the shear-stress field in plane 8 (Fig. 6e), the vortex being much flatter and the point of maximum shear-stress magnitude occurring much closer to the wing than in the measurements. As indicated by the histograms (Fig. 7e), the k-ε model

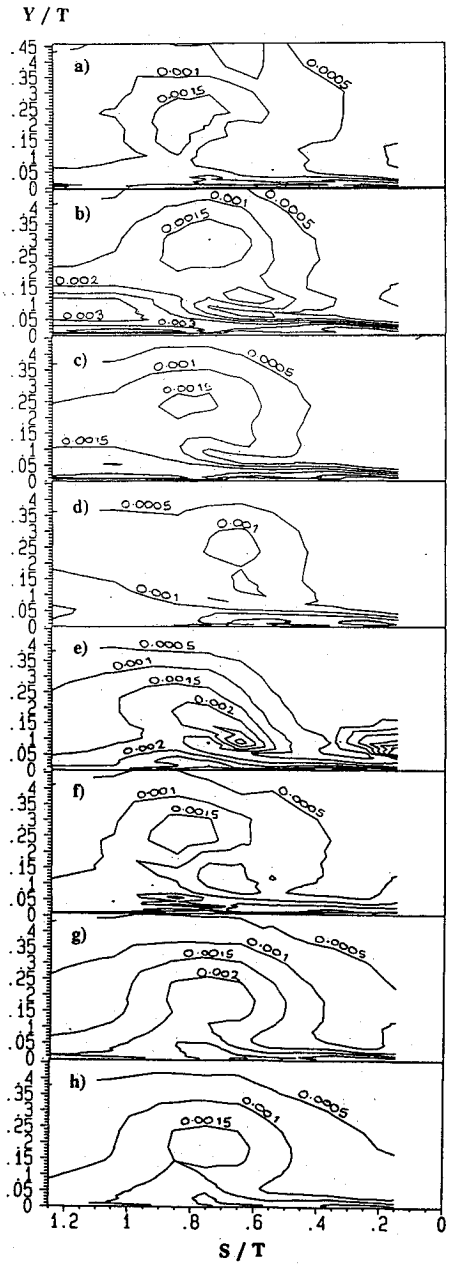

Fig. 6 Contours of measured and computed turbulence shear-stress magnitude $\sqrt{(\overline{uv}^2 + \overline{vw}^2)}/U_{ref}^2$ in plane 8: a) measurements; b) basic mixing-length model; c) Cebeci-Smith model; d) Johnson-King model; e) k-ε model; f) algebraic-stress model; g) Bradshaw's model a_1 = 0.15; h) Bradshaw's model a_1 = 0.11.

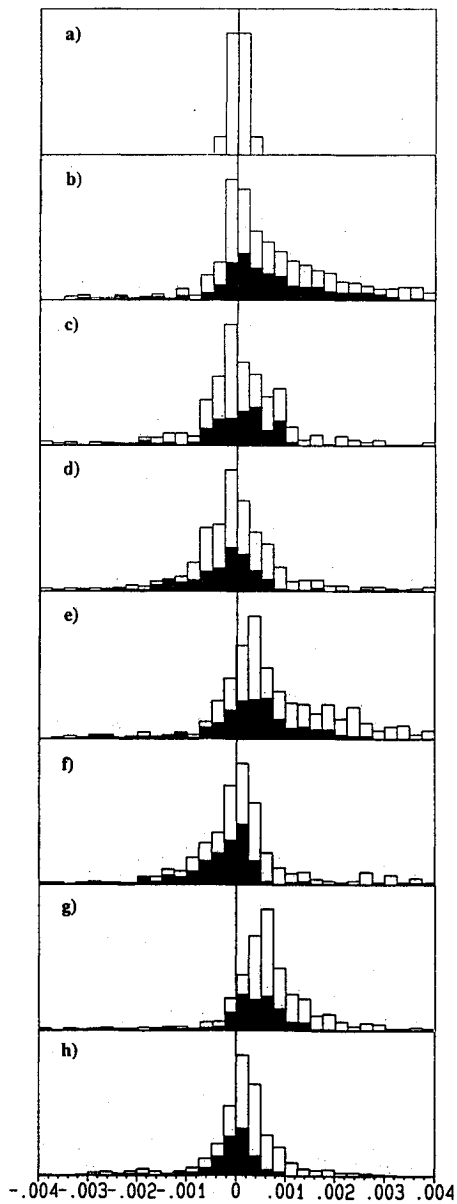

Fig. 7 Histograms of the difference between computed and measured shear-stress magnitudes normalized on U_{ref}^2; filled portion compiled from points outside the line of separation: a) measurements; b) basic mixing-length model; c) Cebeci-Smith model; d) Johnson-King model; e) k-ε model; f) algebraic-stress model; g) Bradshaw's model a_1 = 0.15; h) Bradshaw's model a_1 = 0.11.

Table 2 Mean and rms differences between calculated and measured shear-stress magnitudes computed from 1) all points, and 2) points outside the separation line only

Model	All points[a]		Outside separation[a]	
	Mean	rms	Mean	rms
Measurements	—	0.16		
Basic mixing length	0.64	1.22	0.55	1.07
Cebeci-Smith	0.06	1.03	−0.05	0.77
Johnson-King	0.00	1.05	−0.15	0.96
k-ε	0.72	1.21	0.28	1.01
Algebraic stress	0.09	1.05	−0.30	0.79
Bradshaw, $a_1 = 0.15$	0.62	0.95	0.30	0.74
Bradshaw, $a_1 = 0.11$	0.14	0.84	−0.12	0.63

[a]Error × 1000.

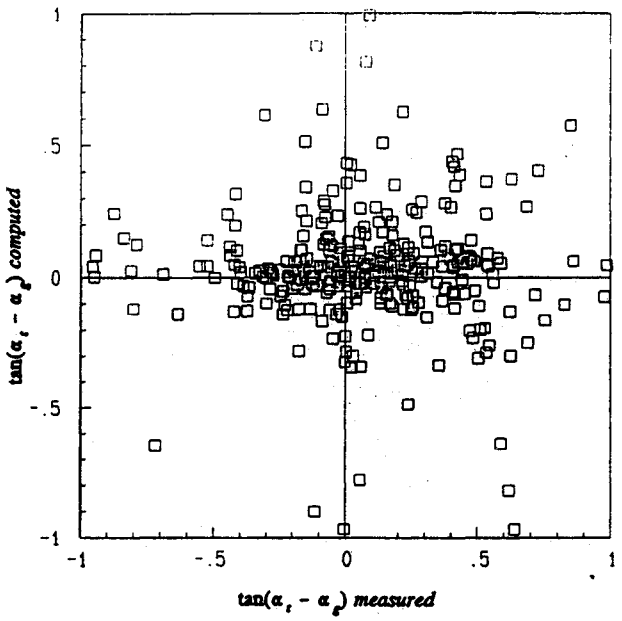

Fig. 8 Comparison of angles between the turbulence shear-stress and mean-velocity gradient vectors obtained from measurements and computed using the algebraic-stress model.

also does poorly in the other planes, the overall mean and rms errors in its predictions being +0.00073 and 0.0012, respectively.

Using Bradshaw's constant of proportionality between the shear-stress magnitude and turbulence kinetic energy produces better qualitative agreement with the experimental data in plane 8. However, it overestimates the shear-stress magnitude at most locations (Fig. 6g). This simple relationship seems unable to account for the low shear-stress levels in the region adjacent to the wing where the vortex is bringing low-turbulence fluid down close to the wall. As shown by the histograms (Fig. 7g), the shear-stress magnitude is also overpredicted in other planes, the mean and rms errors being +0.0006 and 0.00095 overall. These errors can be reduced somewhat by optimizing the value of a_1 (see Figs. 6h and 7h). A value of 0.11 seems to best suit the present data set.

The algebraic-stress model, perhaps the best of these three, produces the most realistic shear-stress contours in plane 8 (Fig. 6f), especially away from the wall. Overall comparisons with shear-stress measurements in other planes (Fig. 7f and Table 2) give negligible mean error and an rms error of 0.00105 overall. Theoretically, at least, the algebraic-stress model is capable of predicting leads and lags in the angle of the shear-stress vector relative to the mean-velocity gradient vector. As shown in Fig. 8, lag angle predictions appear much smaller than, and largely uncorrelated with, measured angles.

Conclusions

New velocity measurements, made in the flow past a wing-body junction, have been presented. Combined with earlier results, these show the formation and development of the horseshoe vortex and its three-dimensional turbulence structure around the entire wing.

A number of turbulence models have been examined using these data. Many of these models require or imply a relationship between the angles of the turbulence shear-stress and mean-velocity vectors. In the present flow, these angles are not only different but do not follow any simple relationship. To predict the shear-stress angle, accurate modeling of the full shear-stress transport equations is clearly needed. In particular, new models based on measurements are needed for the pressure-strain term.

The assumptions of several prescribed eddy-viscosity models, the k-ε model, an algebraic-stress model, and Bradshaw's[17] model, have been tested. For each model, predictions of the magnitude of the shear-stress vector from the measured mean-velocity or turbulence kinetic energy distributions were compared with measurements. The Cebeci-Smith and the algebraic-stress models are amng the best, The k-ε model does not appear suited to this vortical flow.

All of the experimental data presented and referred to here are available in tables and on magnetic disk from the authors.

Acknowledgments

This work was sponsored by the Naval Sea Systems Command through Naval Service Weapons Center Contract N00014-87-K-0421. The authors would like to thank S. Olcmen and A. Obst for their help in taking some of the measurements.

References

[1]Devenport, W. J., and Simpson, R. L., "Some Time-Dependent Features of Turbulent Appendage-Body Juncture Flows," *Proceedings of the 16th Symposium on Naval Hydrodynamics*, National Academy Press, Washington, DC, 1986, pp. 312–335.

[2]Devenport, W. J., and Simpson, R. L., "Turbulence Structure Near the Nose of a Wing-Body Junction," AIAA Paper 87-1310, June 1987.

[3]Devenport, W. J., and Simpson, R. L., "The Turbulence Structure Near an Appendage-Body Junction," *Proceedings of the 17th Symposium on Naval Hydrodynamics*, National Academy Press, Washington, DC, 1988, pp. 461–473.

[4]Devenport, W. J., and Simpson, R. L., "LDV Measurements in the Flow Past a Wing-Body Junction," *4th International Symposium on Applications of Laser Anemometry to Fluid Mechanics*, Instituto Superior Tecnico, Lisbon, Portugal, 1988.

[5]Devenport, W. J., and Simpson, R. L., "Time-Dependent Structure in Wing-Body Junction Flows," *Turbulent Shear Flows 6*, Springer-Verlag, Berlin, Germany, 1988, pp. 232–248.

[6]Devenport, W. J., and Simpson, R. L., "Time-Dependent and Time-Averaged Turbulence Structure Near the Nose of a Wing-Body Junction," *Journal of Fluid Mechanics*, Vol. 210, 1990, pp. 23–55.

[7]Devenport, W. J., and Simpson, R. L., "An Experimental Investigation of the Flow Past an Idealized Wing-Body Junction: Final

Report," Virginia Polytechnic Inst. and State Univ., Blacksburg, VA, VPI-AOE-172, July 1990.

[8]Ahn, S., "Unsteady Features of Turbulence Boundary Layers," M.S. Thesis, Dept. of Aerospace and Ocean Engineering, Virginia Polytechnic Inst. and State Univ., Blacksburg, VA, 1986.

[9]Simpson, R. L., and Barr, P. W., "Laser Doppler Velocimeter Signal Processing Using Sampling Spectrum Analysis," *Review of Scientific Instruments*, Vol. 46, 1975, pp. 835–837.

[10]Durst, F., Melling, A., and Whitelaw, J. H., *Principles and Practice of Laser Doppler Anemometry*, Academic, New York, 1981.

[11]Johnston, J. P., "Measurements in a Three-Dimensional Turbulent Boundary Layer Induced by a Swept Forward-Facing Step," *Journal of Fluid Mechanics*, Vol. 42, Pt. 4, 1970, pp. 823–844.

[12]van den Berg, B., and Elsenaar, A., "Measurements in a Three-Dimensional Incompressible Turbulent Boundary Layer in an Adverse Pressure Gradient Under Infinite Swept Wing Conditions," National Aerospace Lab., Amsterdam, The Netherlands, TR-72092U, 1972.

[13]Fernholz, H. H., and Vagt, J. D., "Turbulence Measurements in an Adverse Pressure Gradient Three Dimensional Turbulent Boundary Layer Along a Circular Cylinder," *Journal of Fluid Mechanics*, Vol. 111, 1981, pp. 233–269.

[14]Rotta, J. C., "A Family of Turbulence Models for Three-Dimensional Thin Shear Layers," *Symposium on Turbulent Shear Flows*, Pennsylvania State Univ., University Park, PA, 1977.

[15]Rodi, W., *Turbulence Models and Their Application in Hydraulics—A State of the Art Review*, 2nd ed., International Association for Hydraulic Research, Delft, The Netherlands.

[16]van den Berg, B., "Some Notes on Three-Dimensional Turbulent Boundary-Layer Data and Turbulence Modelling," *Three-Dimensional Turbulent Boundary Layers*, Springer-Verlag, Berlin, Germany, 1982, pp. 1–18.

[17]Bradshaw, P., "Calculation of Three-Dimensional Turbulent Boundary Layers," *Journal of Fluid Mechanics*, Vol. 46, 1971, pp. 417–445.

[18]Abid, R., "Extension of the Johnson-King Turbulence Model to the 3-D Flows," AIAA Paper 88-0223, Jan. 1988.

[19]Chen, H. C., and Patel, V. C., "Near-Wall Turbulence Models for Complex Flows Including Separation," *AIAA Journal*, Vol. 26, No. 6, 1988, pp. 641–648.

[20]Deng, G., "Resolution des equations Navier Stokes tridimensionelles. Application au calcul d'un raccord plaque plane-alle," Ph.D. Dissertation, Universite de Nantes, France, 1989.

[21]Abid, R., and Schmitt, R., "Critical Examination of Turbulence Models for a Separated Three Dimensional Turbulent Boundary Layer," *Recherches Aérospatiales*, No. 6, 1984, pp. 385–401.

[22]Launder, B. E., "A Generalized Algebraic Stress Transport Hypothesis," *AIAA Journal*, Vol. 20, No. 3, 1982, pp. 436, 437.